Lab on a Chip

PAPER

View Article Online
View Journal

Cite this: DOI: 10.1039/d3lc01084h

High-performance magnetic metal microrobot prepared by a two-photon polymerization and sintering method†

Rui Li,‡[a] Modong Jiang,‡[a] Bingrui Liu,[a] Shaojun Jiang,[a] Chao Chen,[b] Mengxue Liang,[c] Lijie Qu,[a] Chaowei Wang,[a] Gang Zhao,[a] Yanlei Hu,[a] Dong Wu,[a] Jiaru Chu[a] and Jiawen Li*[a]

Magnetically-actuated microrobots (MARs) exhibit great potential in biomedicine owing to their precise navigation, wireless actuation and remote operation in confined space. However, most previously explored MARs unfold the drawback of hypodynamic magnetic torque due to low magnetic content, leading to their limited applications in controlled locomotion in fast-flowing fluid and massive cargo carrying to the target position. Here, we report a high-performance pure-nickel magnetically-actuated microrobot (Ni-MAR), prepared by a femtosecond laser polymerization followed by sintering method. Our Ni-MAR possesses a high magnetic content (~90 wt%), thus resulting in enhanced magnetic torque under low-strength rotating magnetic fields, which enables the microrobot to exhibit high-speed swimming and superior cargo carrying. The maximum velocity of our Ni-MAR, 12.5 body lengths per second, outperforms the velocity of traditional helical MARs. The high-speed Ni-MAR is capable of maintaining controlled locomotion in fast-flowing fluid. Moreover, the Ni-MAR with massive cargo carrying capability can push a 200-times heavier microcube with translation and rotation motion. A single cell and multiple cells can be transported facilely by a single Ni-MAR to the target position. This work provides a scheme for fabricating high-performance magnetic microrobots, which holds great promise for targeted therapy and drug delivery *in vivo*.

Received 17th December 2023,
Accepted 1st January 2024

DOI: 10.1039/d3lc01084h

rsc.li/loc

Introduction

Magnetically-actuated microrobots (MARs), emerging as a favorable tool in targeted therapy[1–4] and precise medicine,[5,6] have become promising candidates for the next generation of cancer treatment. In the past decades, significant advancements have been made in the fabrication,[7–10] actuation[11] and functionalization[12] of magnetic microrobots. These microrobots have been designed in diverse morphologies, such as tubular,[13] helical[14] and spherical shapes.[15] Among them, helical microrobots, propelled by a low-strength rotation magnetic field, have aroused increasing attention due to their precise locomotion in three-dimensional (3D) narrow and confined spaces.[16,17] Under a uniform rotating magnetic field, a magnetic torque (T_m) is generated to rotate helical microrobots, and the rotation of the microrobots results in forward propulsion force and drilling. However, current helical microrobots are faced with the challenge of further increasing the magnetic torque, thus restricting the microrobots to swimming in stagnant or low-velocity fluidic environments and carrying a small amount of cargo to the target position. Although enlarging the strength of the magnetic field (B) can enhance the magnetic torque, it is extremely energy-consuming to maintain a suitable 3D working place with high strength. In contrast, increasing the internal magnetic content (M) of helical microrobots enables the magnetic torque to be boosted efficiently while reducing the energy consumption. Hence, the production of helical microrobots with high magnetic content and enhanced magnetic torque can significantly improve the swimming performance and will find applications in controllable locomotion in fast-flowing fluid (*e.g.*, bloodstream) and massive cargo (*e.g.*, drugs and cells) carrying to the lesion location.

Various methods have been reported to produce helical microrobots. For example, template-based deposition uses natural[18] and artificial[19] templates followed by vapor deposition[20] and electrodeposition[21] of magnetic materials to

[a] CAS Key Laboratory of Mechanical Behavior and Design of Materials, Key Laboratory of Precision Scientific Instrumentation of Anhui Higher Education Institutes, Department of Precision Machinery and Precision Instrumentation, University of Science and Technology of China, Hefei 230027, China. E-mail: jwl@ustc.edu.cn
[b] Department of Materials Physics and New Energy Device, School of Materials Science and Engineering, Hefei University of Technology, Hefei 230009, China
[c] CAS Key Laboratory of Urban Pollutant Conversion, Department of Environmental Science and Engineering, University of Science and Technology of China, Hefei 230026, China

† Electronic supplementary information (ESI) available. See DOI: https://doi.org/10.1039/d3lc01084h

‡ These authors contributed equally to this paper.

prepare helical microrobots. However, the existence of templates poses a challenge in further increasing the magnetic content of microrobots. Although strategies relying on self-scrolling[22] and glancing angle deposition (GLAD)[23] can generate helical microrobots with high magnetic content, they encounter difficulties owing to low production speed and complex fabrication steps. Recently, femtosecond direct laser writing (fs-DLW), featuring excellent processing flexibility and 3D geometry designability, has evolved as a compelling tool for magnetic helical microrobot fabrication.[24,25] Based on two-photon polymerization, fs-DLW is mainly employed for constructing organic polymer microrobots decorated with magnetic materials.[1,26–33] The direct construction of pure magnetic microrobots while maintaining their 3D fabrication capacity is a crucial issue for the current fs-DLW technology. Therefore, seeking a facile strategy for producing helical microrobots with high magnetic content, thereby allowing for controlled locomotion in high-speed flows and strong carrying capabilities, is still a challenge and an urgent requirement.

Here, we develop a "two-photon polymerization + sintering" method to fabricate a pure-nickel magnetically-actuated microrobot (Ni-MAR) with high magnetic content (~90 wt%) and diverse 3D biomimetic morphologies. Based on its high magnetic content, our Ni-MAR with enhanced magnetic torque is capable of high-speed swimming in static liquid and superior cargo carrying to the target position. The maximum velocity of the Ni-MAR is 12.5 body lengths per second under low-strength rotating magnetic fields (<10 mT), much faster than current helical microrobots fabricated by fs-DLW. A massive microcube (200 times the weight of the microrobot) is pushed by a single swimming Ni-MAR and realizes translation and rotation motion, which has not been reported before. Finally, as a proof-of-concept demonstration, the high-speed Ni-MAR displays controllable locomotion in fast-flowing fluid within a microfluidic channel, offering an alternative scheme for microrobot propulsion in bloodstream. In addition, multiple cells are carried by a single Ni-MAR to the target position, which will significantly improve the microrobot's cargo carrying and therapeutic efficiency.

Results and discussion

Fs-DLW followed by sintering and reduction to produce pure Ni-MARs

Fig. 1a shows the fabrication of pure Ni-MARs, which mainly includes two procedures: the sculpture of

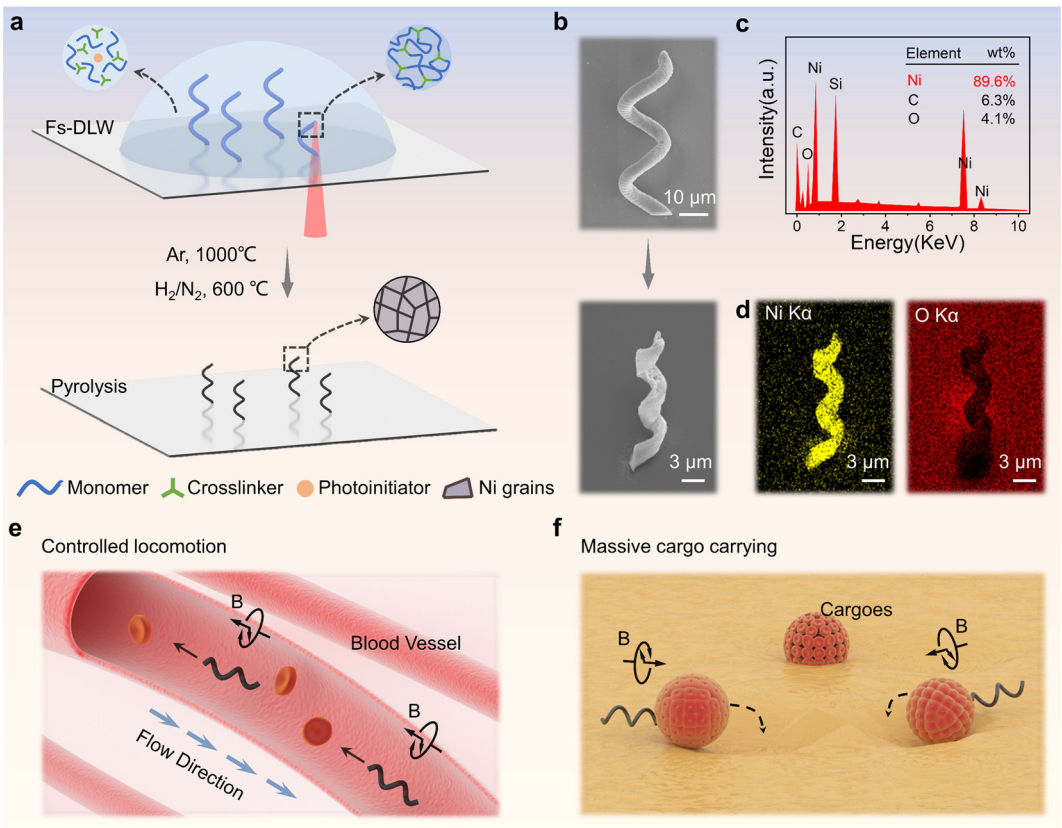

Fig. 1 Femtosecond laser direct writing (fs-DLW) followed by sintering and reduction to produce a nickel magnetically-actuated microrobot (Ni-MAR). (a) Fs-DLW of the polymer-based nickel-containing microhelix, followed by high-temperature sintering and reduction to obtain the Ni-MAR. (b) The SEM images of the polymer-based microhelix and Ni-MAR. (c) Energy dispersive spectroscopy (EDS) spectrum showing the Ni-MAR containing ~90 wt% of nickel. (d) EDS elemental maps of the Ni-MAR. (e) Ni-MAR with high magnetic content capable of high-speed swimming, thus allowing for controlled locomotion in fast-flowing fluid (*e.g.*, bloodstream). (f) Ni-MAR with high magnetic content holding outstanding cargo-carrying capability, which can deliver massive cargoes or cells to the target position.

polymer-based nickel-containing microhelices utilizing fs-DLW, and then high-temperature sintering and reduction to obtain pure Ni-MARs. Initially, organic–inorganic nickel-containing photoresin is prepared[34] and dropped onto a heat-resisting glass substrate. Then, the polymer-based microhelices are sculpted using a fs-DLW system (Fig. S1a†), followed by immersing in ethanol solution to develop for 30 min. Finally, the Ni-MARs are obtained after the polymer-based microhelices are sintered at 1000 °C under an argon flow and then reduced at 600 °C under reducing gases (5% H_2 and 95% N_2, Fig. S1b†). Thermogravimetry analysis (TGA)-differential scanning calorimetry (DSC) is performed to optimize the heating profile, as shown in Fig. S2.† Owing to the pyrolysis of organic components and crystallization of Ni grains during the thermal treatment, the microhelices undergo a dramatic volume shrinkage of about 80% (Fig. 1b and S3†).

We perform energy dispersive X-ray spectroscopy (EDS) analysis to verify that the Ni-MARs have high nickel content. After excluding the silicon and oxygen elements from the glass substrate, the content of nickel inside the Ni-MAR reaches 89.6 wt% (Fig. 1c and S4†). Besides, the uniform element distribution in the EDS maps (Fig. 1d) also confirms that there is no obvious nickel separation and enrichment phase inside the microrobot. Ni-MARs with high-content magnetic materials are capable of strongly responding to an external magnetic field. In order to measure the magnetization of Ni-MARs, a vibrating sample magnetometer (VSM) is used with a VSM loop shown in Fig. S5.†

Due to the high Ni content and robust magnetization, the Ni-MARs are endowed with strong magnetic torque. The magnetic torque T acting on a microrobot is[35]

$$T = V{\cdot}M \times B$$

where V is the volume of the magnetic material and M is the magnetization. B is the external magnetic field. Therefore, an increase in magnetic content results in a larger volume V, which consequently leads to a stronger magnetic torque. Our Ni-MARs with enhanced magnetic torque are capable of high-speed swimming and strong cargo carrying, and have potential applications for controlled locomotion in fast flowing fluid (*e.g.*, bloodstream) and pushing massive cargoes (*e.g.*, drugs or cells) to the target position. As a proof of concept, Fig. 1e is a schematic diagram of a Ni-MAR swimming upstream against the fast-flowing blood in a capillary, which indicates that our Ni-MAR has potential to swim controllably in the bloodstream. Fig. 1f shows another sketch map of a Ni-MAR pushing massive cargoes (much bigger and heavier than the microrobot) to the target position, which suggests the strong load-carrying capacity of our Ni-MAR. These proof-of-concept demonstrations offer feasible technical routes for targeted therapy *in vivo* in the future clinical medicine.

Fabrication of polymorph Ni-MARs with designed 3D geometric shape

Owing to the dramatic shrinkage during the high-temperature sintering and reduction process, pyrolytic microstructures are prone to have structural distortions and are difficult to hold their original shapes. Therefore, we develop a pedestal-free sintering method, based on structure design and fabrication parameter optimization, to generate polymorph Ni-MARs with high fidelity.

Fig. 2a demonstrates the design and optimization principle. In the structure design, to minimize the shrinking stress and shape distortion, we fabricate an upstanding microhelix with minimum contact area between the structure and substrate. For comparison, microhelices with different contact forms are fabricated and pyrolyzed as shown in Fig. S6.† These microhelices are all distorted after sintering, and only the upstanding microhelix can maintain its morphology with high fidelity. In the fabrication parameter optimization, the radius (R) and the pitch (P) of the polymer-based microhelix (before sintering) have a decisive effect on the morphology of pyrolytic microhelices (after sintering). Therefore, we explore the impact of varied radius (3–9 μm) and pitch (20–50 μm) of the polymer-based microhelix on the morphology of pyrolytic microhelices, with details illustrated in Fig. S7.† According to these morphologies, we define a shape parameter (SP) to divide these microhelices into three categories (I, II, III) (Note S1†). Fig. 2b shows the SEM images of microhelices with three types, where type I (SP $>$ 7) is slim, type II (7 $>$ SP $>$ 3) is moderate and type III (SP $<$ 3) is dumpy. The preliminary actuation experiment of the three types of microhelices under a rotating magnetic field finds that type II has a superior swimming performance and is chosen in the following experiments. Therefore, after the structure design and parameter optimization, pyrolytic microhelices with minimum shape distortion and high fidelity are obtained controllably and robustly.

To demonstrate the fabrication capability of our method, diverse helical microstructures with more complicated morphologies are designed and fabricated according to this principle. Fig. 2c–f show four kinds of typical helical microstructures, including conical microhelix, double microhelix, single microhelix with a head, and double microhelix with a head. These microhelices, which undergo insignificant shape distortion after pyrolysis, all keep high-fidelity morphologies.

High-speed swimming behavior of Ni-MARs

Ni-MARs with high nickel content and superior magnetization can move rapidly in a stagnant liquid environment under an external rotating magnetic field, which is generated by Helmholtz electromagnets (Fig. 3a). Here, we explore the Ni-MAR's swimming velocity with the increase of the frequency of the magnetic field and the viscosity of liquid.

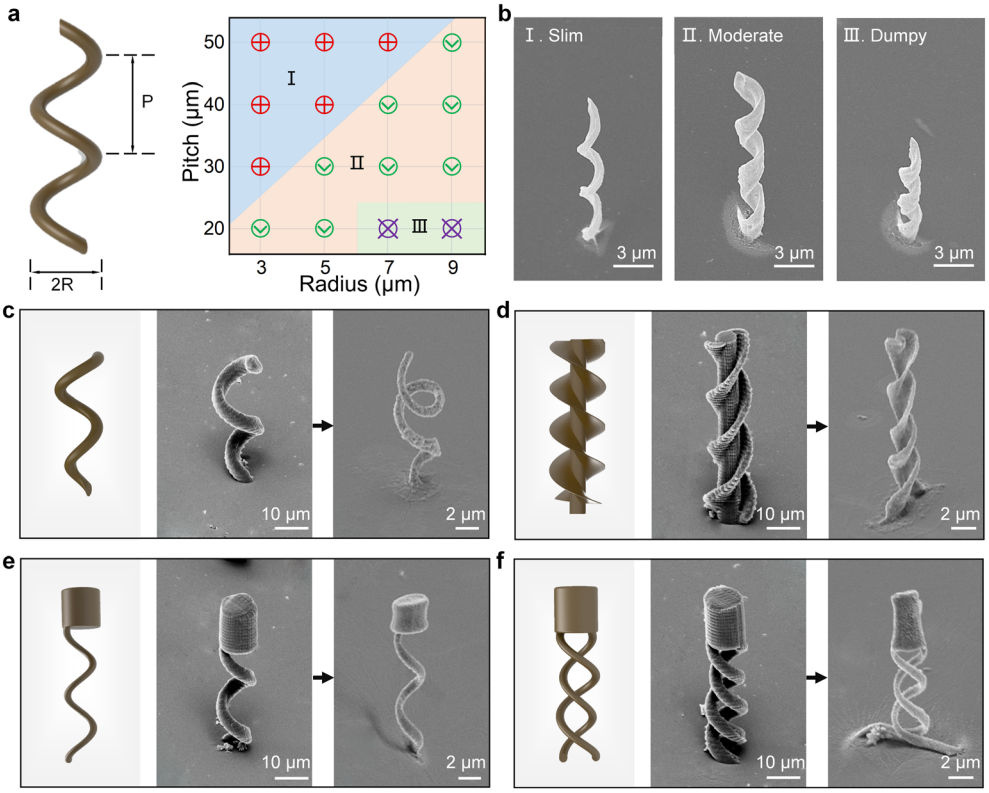

Fig. 2 Fabrication of polymorph Ni-MARs with designed 3D geometric shape. (a) The structure design and parameter optimization principle for pedestal-free sintering of the Ni-MAR. The morphology of Ni-MARs (type I, II, III) after sintering is determined by the radius and pitch of polymer-based microhelices before sintering. (b) The SEM images of the three types of pyrolytic Ni-MARs. Type I is slim; type II is moderate; type III is dumpy. (c–f) Fabrication of Ni-MARs with different 3D morphologies based on the design and optimization principle, including conical microhelix, double microhelix, single microhelix with a head and double microhelix with a head. The three images, from left to right, show the schematic diagram and SEM images of polymer-based microhelices and pyrolytic Ni-MARs.

As shown in Fig. 3b, the swimming modes of our Ni-MARs transforms from wobbling motion to corkscrewing motion and to a step-out condition with the increase of frequency. In addition, this transformation also occurs when the liquid viscosity increases while the frequency remains unchanged. Fig. 3c–h demonstrate the experimental results of our Ni-MAR's swimming velocity and mode changing with the frequency of the magnetic field and the viscosity of liquid. The Ni-MAR is first actuated in deionized (DI) water (0.8 CP viscosity) and its swimming velocity varies as the frequency increases (Fig. 3c). During the whole actuation process, the strength of the external magnetic field is fixed at 2.3 mT. v_t, v_f and v_d represent the total velocity, forward velocity and drift velocity of the Ni-MAR, respectively. The motion mode of the Ni-MAR keeps wobbling when the frequency is less than 60 Hz. As the frequency increases, a wobbling-to-corkscrew transformation occurs. In the meantime, the velocity of the Ni-MAR continuously increases until a maximum velocity of 12.5 body lengths per second (BL s^{-1}) appears when the frequency reaches 220 Hz (orange star). It is worth noting that this maximum velocity is far beyond the velocity of conventional helical microrobots fabricated by fs-DLW. After that, a sharp fall is witnessed in the plot because the Ni-MAR is in a step-out condition and loses its velocity.

According to the slender body theory, the step-out frequency ($f_{||}$) relies on three main factors including the helix geometry, material category and magnetic properties, which can be formulated as[36]

$$f_{\parallel} = \frac{A(1+\gamma^2)}{8\gamma\pi}\sin 2\alpha$$

where A is a characteristic parameter, which has positive correlations with the magnetization of microrobots. γ is a steerability parameter depending on the microhelix geometry and a is the misalignment angle. Therefore, we can conclude that $f_{||}$ is positively correlative to the microrobot's magnetization. $f_{||}$ means the highest frequency when the microrobot maintains synchronous rotation with the external magnetic field. Our Ni-MAR with high nickel content and superior magnetization has an extra-high $f_{||}$, thus accounting for a much higher swimming velocity than conventional helical microrobots.

The swimming trajectory of the Ni-MAR in DI water at the highest velocity is shown in Fig. 3d. There exists a considerable drift motion in the Ni-MAR's swimming trajectory. We hold that the high density of the Ni-MAR in

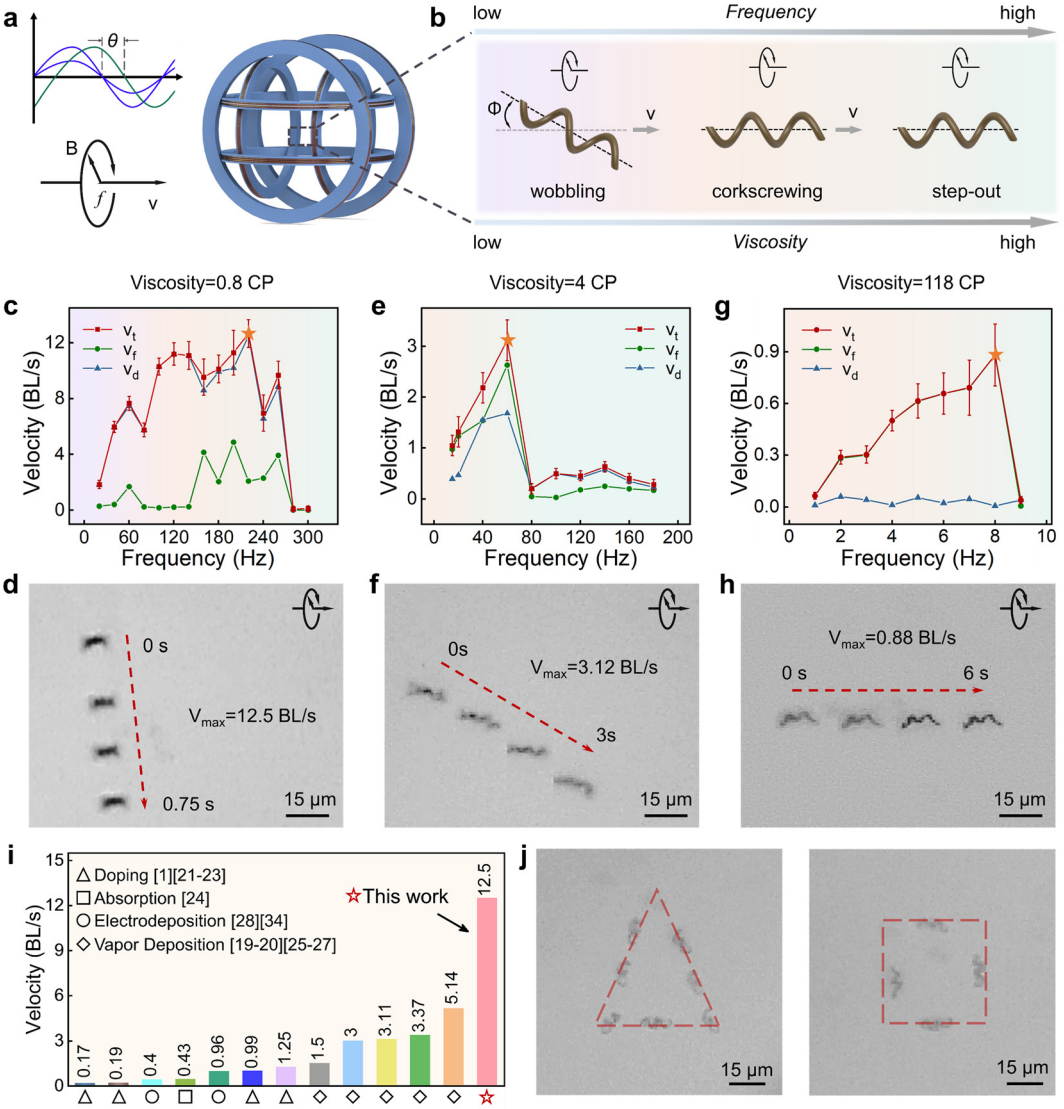

Fig. 3 The high-speed swimming behavior of the Ni-MAR under a rotating magnetic field. (a) Schematic of the magnetic field generator. The electrical signal is inputted into the Helmholtz coils to generate a rotating magnetic field. (b) The Ni-MAR showing different swimming modes: the wobbling, corkscrewing and step-out, with the increase of the frequency of the magnetic field and the viscosity of liquid. (c and d) The swimming velocity of the Ni-MAR in DI water (viscosity 0.8 CP) *versus* the frequency, and the swimming trajectory of the Ni-MAR at the maximum velocity (12.5 BL s^{-1}) under the magnetic field at 2.3 mT and 220 Hz. (e and f) The swimming velocity of the Ni-MAR in viscous liquid (viscosity 4 CP) *versus* the frequency, and the swimming trajectory of the Ni-MAR at the maximum velocity (3.12 BL s^{-1}) under the magnetic field at 2.3 mT and 60 Hz. (g and h) The swimming velocity of the Ni-MAR in viscous liquid (viscosity 118 CP) *versus* the frequency, and the swimming trajectory of the Ni-MAR at the maximum velocity (0.88 BL s^{-1}) under the magnetic field at 10 mT and 8 Hz. (i) Comparison of the swimming velocity of the Ni-MAR and previously reported helical microrobots fabricated by fs-DLW. (j) Triangle-shaped and square-shaped swimming trajectories of the Ni-MAR controlled by the magnetic field.

low-viscosity solution results in strong interaction between the Ni-MAR and the substrate, thus causing the drift motion.

Compared with DI water, real blood has a higher liquid viscosity (~4 CP).[37,38] Hence, to simulate the swimming performance of the Ni-MAR in real blood, we perform an actuation experiment of the Ni-MAR *versus* the frequency of the magnetic field in moderate-viscosity liquid (~4 CP). Glycerite is added to increase the viscosity of liquid[39] (Note S2†). Fig. 3e depicts that the Ni-MAR starts with a wobble-free corkscrew propulsion and its velocity increases with the increase of frequency. A maximum velocity of 3.12 BL s^{-1} is observed at 60 Hz (orange star). Then the step-out condition is reached and the velocity drops dramatically. The strength of the external magnetic field is 2.3 mT during the whole process. Fig. 3f shows the swimming trajectory of the Ni-MAR in viscous liquid (~4 CP) at the highest velocity. Compared with the swimming characteristics in DI water, the Ni-MAR in moderate-viscosity liquid (~4 CP) demonstrates a lower step-out frequency and velocity, but a smaller drift motion. Actually, for real blood, which is comprised of plasma and other components (*e.g.*, red cells), the swimming situation of the Ni-MAR in blood is extraordinarily complicated.[40] This is a simple simulated

experiment by actuating the Ni-MAR in moderate-viscosity liquid, without considering the interaction between the Ni-MAR and other blood components. Nevertheless, our result can be a guideline to design and conduct the swimming experiment of microrobots in real blood in the future.

As the viscosity increases from 4 CP to 118 CP, the drifting effect of the Ni-MAR gradually decreases until it completely disappears. As shown in Fig. 3g, the positive correlation between the velocity and frequency is maintained until the velocity peaks at 0.88 BL s^{-1} when the frequency is 8 Hz. In particular, the current state-of-the-art metallic helical microrobots in the same viscous liquid (118 CP) have a maximum velocity of 0.4 BL s^{-1}.[33] Our Ni-MAR swims two times faster than them. What's more, the Ni-MAR swims forward with no drift motion throughout the whole process. Fig. 3h demonstrates the swimming trajectory of the Ni-MAR at maximum velocity. A bigger magnetic field strength of 10 mT is needed to actuate the Ni-MAR to swim in such a high viscosity solution. Details about the swimming performance of the Ni-MAR in viscous liquids are shown in Movie S1.†

We make a comparison between the velocities of our Ni-MAR and previously reported helical microrobots fabricated by fs-DLW (Fig. 3i) and find that our Ni-MAR outperforms them. Currently existing helical microrobots utilize fs-DLW to sculpt their templates followed by various post-processing methods (*e.g.*, electrodeposition,[33,41] doping,[1,26–28] absorption,[29] and vapor deposition[24,25,30–32]) to enhance their magnetism. However, these microrobots are unable to further increase their magnetic content and swimming speed, which is determined by the inherent properties of their process methods. By contrast, our Ni-MAR with nickel as its body material (~90 wt%) is capable of high-frequency response to the external rotating magnetic field, thus exhibiting a higher speed. Furthermore, the Ni-MAR is actuated along some specific routes to demonstrate the steerability under the magnetic field. As shown in Fig. 3j, "triangle" and "square" patterns are realized. The controllability of the Ni-MAR is demonstrated in Fig. S8, S9 and Movie S2.†

Controllable swimming of the Ni-MAR in fast-flowing fluid

The vascular system can carry nutrients and oxygen *via* the fast-flowing bloodstream throughout the body.[42] For clinical applications, microrobots entering the bloodstream can

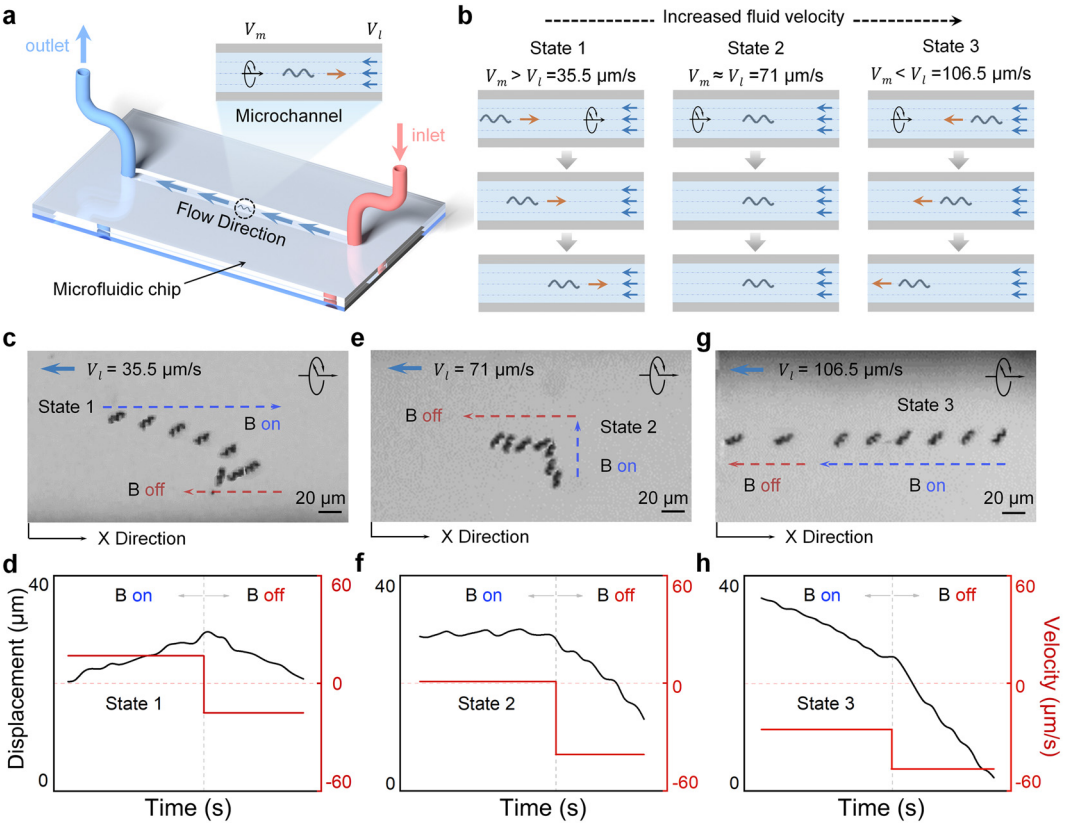

Fig. 4 Controllable swimming of the Ni-MAR in fast-flowing fluid. (a) Schematic of the controllable swimming of the Ni-MAR in a microfluidic chip with flowing liquid. v_m denotes the maximum velocity of the Ni-MAR in static viscous liquid (4 CP) and v_l represents the velocity of flowing liquid. The blue arrow indicates the direction of fluid while the orange arrow signifies the moving direction of the Ni-MAR in the microchannel. (b) Three states of the Ni-MAR in a microfluidic channel with different fluid velocities. State 1: $v_m > v_l$ = 35.5 μm s^{-1}, swimming upstream against the flowing fluid. State 2: $v_m \approx v_l$ = 71 μm s^{-1}, keeping still in the flowing fluid. State 3: $v_m < v_l$ = 106.5 μm s^{-1}, swimming downstream along the flowing fluid. (c, e and g) The swimming trajectories of the Ni-MAR in low-, moderate- and high-velocity fluid after *B* on and *B* off, respectively. (d, f and h) The displacements and velocities of the Ni-MAR at the *X* direction in low-, moderate- and high-velocity fluid after *B* on and *B* off, correspondingly.

deliver drugs and cells effectively to the lesion position. However, the controllable locomotion of current microrobots in fast-flowing bloodstream is still a challenge. Our Ni-MAR with a high-speed swimming merit could offer a scheme to make this vision come true.

To simulate the swimming performance of Ni-MARs in blood vessels, we perform actuation tests of the Ni-MAR in a microfluidic channel with flowing liquid (Fig. 4a, and S10†). The viscosity of the fluid is 4 CP, which is similar to the viscosity of real blood. This microfluidic device is composed of a microfluidic chip and an injection pump. A straight channel, an inlet and an outlet together form the microfluidic chip. The cross section of the channel is a rectangle with 200 μm in width and 250 μm in thickness. By changing the feed rate of the injection pump, the velocity of the flowing fluid in the channel can be adjusted. Here, three fluid velocities (v_l) are set as 35.5 μm s^{-1}, 71 μm s^{-1} and 106.5 μm s^{-1}, which correspond to low-, moderate- and high-velocity fluid, respectively. The Ni-MAR with the maximum velocity (v_m = 3.12 BL s^{-1} in Fig. 3f) is swimming against the flowing fluid. With the increase of fluid velocity, Ni-MARs demonstrate three states (states 1, 2, and 3) as shown in Fig. 4b. In state 1, $v_m > v_l$, the Ni-MAR swims upstream against the flow. In state 2, $v_m \approx v_l$, the Ni-MAR keeps still in the flow. In state 3, $v_m < v_l$, the Ni-MAR swims downstream along the flow.

Fig. 4c shows the swimming trajectory of the Ni-MAR in low-velocity fluid (v_l = 35.5 μm s^{-1}) during the rotating magnetic field (B) on and off. When the B is on, the Ni-MAR swims upstream against the flow (state 1) as the blue dotted line indicates. In the meantime, a positive-slope displacement curve and a positive velocity line in Fig. 4d have revealed this counter-flow swimming process quantitatively. When the B is off, the Ni-MAR goes downstream with the fluid as the red dotted line points (Fig. 4c). Correspondingly, a negative-slope displacement curve and a negative velocity line are shown in Fig. 4d. Here, we only concentrate on the displacement and velocity in the X direction. When the fluid velocity (v_l) increases to 71 μm s^{-1}, the Ni-MAR keeps still in the moderate-velocity flowing fluid (Fig. 4e). Once the B is on, the microrobot remains in state 2 and has no displacement in the X direction. After the B is turned off, the Ni-MAR swims downstream with the fluid. Quantitative statistics about the displacement and velocity are shown in Fig. 4f, where a flat displacement curve and a zero velocity denote that the Ni-MAR keeps still in the fluid, while a negative curve and a negative velocity line signify the downstream swimming of the Ni-MAR. Finally, when the fluid velocity increases to 106.5 μm s^{-1}, the Ni-MAR will always swim downstream whether the B is on or not (Fig. 4g), which can be described by the sustaining negative-slope displacement curve and negative velocity line in Fig. 4h. In state 3, a denser trajectory in the image and a smaller negative velocity in the plot manifest that the Ni-MAR struggles to swim against the flowing fluid but fails. Details about these three types of controllable locomotion in the fast-flowing fluid are shown in Movie S3.†

The above-mentioned controllable swimming of Ni-MARs in flowing fluid with different velocities lays a foundation for the microrobots' future clinical application in fast-flowing bloodstream. The velocity of blood flow *in vivo* ranges from hundreds of micrometers per second in blood capillaries[43] to tens of centimeters per second in arteries.[44] Although the fluid velocity of the above test is lower compared with the velocity of real bloodstream, the length of our Ni-MAR is quite short (less than 20 μm). It is reasonable to expect that with the increase of structure size, our Ni-MAR can dramatically increase its speed and swim upstream in faster fluid.

Exceptional cargo-carrying capability of the Ni-MAR

In nature, there are various outstanding porters, which can carry cargoes much heavier than their weights.[45–47] For instance, the ant is capable of transporting a heavy object, which is hundreds of times its body weight (Fig. 5a). Inspired by this, if the microrobots gain this kind of transportation capability, they will significantly improve the efficiency of targeted drug and cell delivery. Our Ni-MARs with high nickel content provide a promising scheme, because the enhanced magnetic torque can endow them with adequate thrust force to push heavy objects.

Fig. 5b shows that a microcube pushed by a Ni-MAR can realize translation and rotation motion. This 20 μm microcube, made of SZ2080 photoresist and fabricated by fs-DLW, is designed to be about 200 times heavier than the Ni-MAR (Fig. 5c and Note S3†). Although we can print the Ni-MAR with the length range from 1 μm to 200 μm *via* the fs-DLW and sintering method, the Ni-MAR used here has a diameter of 2 μm and a length of 20 μm. We choose these size parameters based on its superior morphology and swimming performance according to the optimization principle. What's more, this 200 times heavier microcube is the heaviest cargo which can be pushed by the Ni-MAR at the frequency of 25 Hz. We establish a theoretical model as shown in Note S4† to explain this.

The directions of the microcube's translation (upward or downward) and rotation (clockwise or counter-clockwise) are determined by the relative position between the long axis of the Ni-MAR and the mass center of the microcube (o). Fig. 5d depicts the upward translation and clockwise rotation of the microcube pushed by a swimming Ni-MAR under a rotating magnetic field. Initially, the axis of the Ni-MAR (thrust direction) is above the mass center of the microcube (o) to generate a clockwise moment and angular velocity (ω). After 28 seconds, the microcube has rotated 90 degrees (Movie S4†). Besides, an upward linear velocity (v) is obtained due to the component of pushing force in the upward direction. By recording the trajectory of the microcube using Tracker software, we acquire the plots of linear velocity and angular velocity of the microcube *versus* time (Fig. 5e). The average linear velocity ($\bar{v}$) and angular velocity ($\bar{\omega}$) are 0.48 μm s^{-1} and 0.043 rad s^{-1}, respectively. In contrast, if the Ni-MAR pushes on the other side, the microcube will move downward and

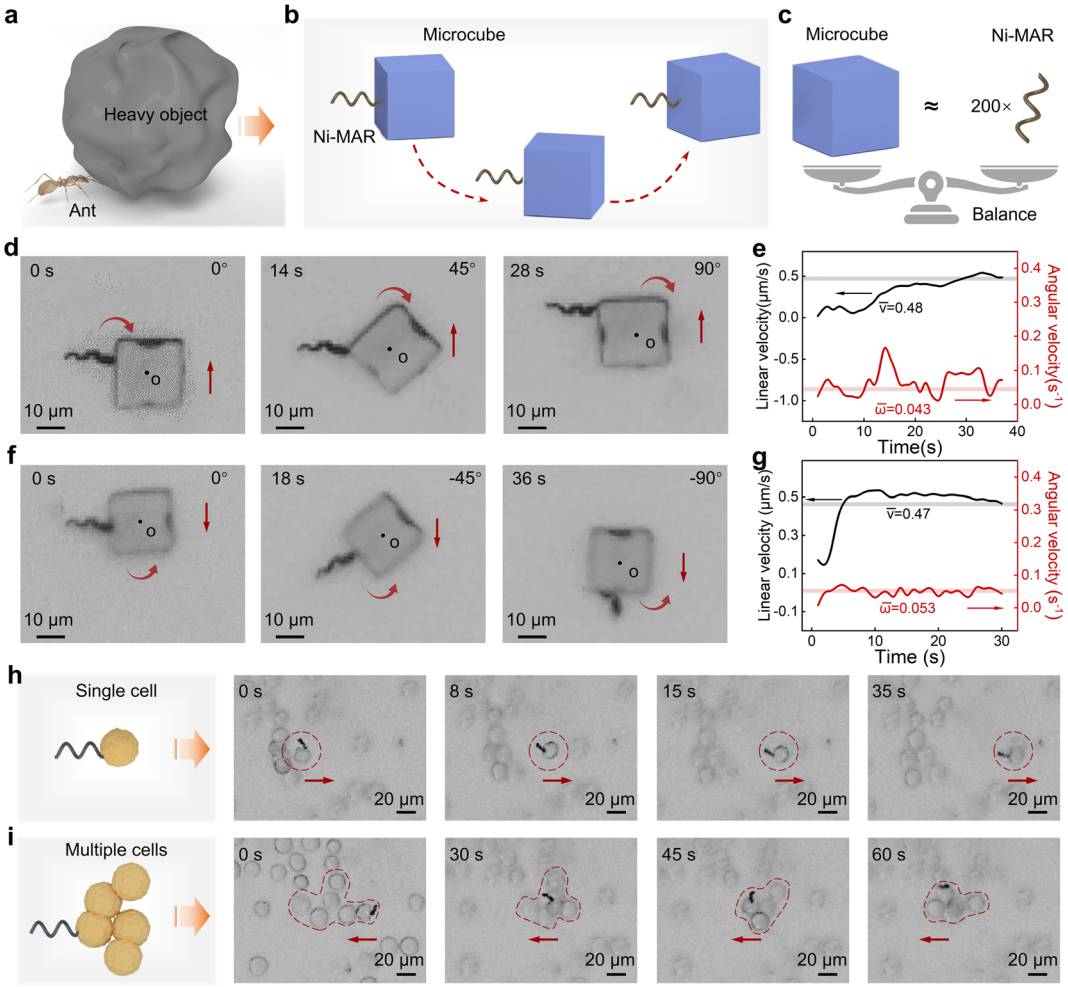

Fig. 5 Exceptional cargo-carrying capability of the Ni-MAR. (a) Schematic diagram of an ant carrying a heavy object hundreds of times heavier than its weight. (b) Schematic diagram of a microcube pushed by a swimming Ni-MAR to realize translation and rotation motion. (c) The microcube weighing about 200 times the Ni-MAR. (d) The close-up images of the microcube's upward translation and clockwise rotation pushed by a swimming Ni-MAR. (e) The linear velocity and angular velocity of the microcube *versus* time. (f) The close-up images of the microcube's downward translation and counter-clockwise rotation pushed by a swimming Ni-MAR. (g) The linear velocity and angular velocity of the microcube *versus* time. (h and i) The schematic diagram and close-up images of a swimming Ni-MAR pushing a single cell and multiple cells to the target position.

counter-clockwise (Fig. 5f), and its average linear velocity and angular velocity are 0.47 μm s^{-1} and 0.053 rad s^{-1}, respectively (Fig. 5g).

In addition, strong transportation capability enables our Ni-MARs to push a single cell or multiple cells to the targeted position with ease. As shown in Fig. 5h, globular HeLa cells are firstly added around the Ni-MAR. Then, the swimming Ni-MAR separates one HeLa cell from others and pushes this cell from left to right. Furthermore, the swimming Ni-MAR is capable of pushing multiple cells, such as six cells together in Fig. 5i, from right to left (Movie S5†). The transportation of so many cells based on this small-sized microrobot can fully demonstrate the robust transportation capability of our Ni-MAR.

Besides, we perform a cell viability test to evaluate the effect of our Ni-MARs on the cells. HeLa cells are first seeded on a glass substrate with a Ni-MAR array fabricated on it and cultured in medium for 48 hours (experimental group). As shown in Fig. S11,† the increased green fluorescence signal indicates that the HeLa cells grow and proliferate normally around the Ni-MAR array. A control group is designed by culturing HeLa cells on a glass substrate without a Ni-MAR array (control group). Quantitative statistics of the fluorescent area in the experimental group and control group demonstrate that the Ni-MAR array has little effect on the HeLa cell viability. Then, a preliminary degradation test is performed by immersing the Ni-MAR array in simulated gastric fluid with a pH of 1.8 for 6 h, and the Ni-MARs gradually degrade and finally disappear. Finally, we evaluate the biocompatibility by exploring the 3D morphology and element content of the Ni-MAR before and after the cell culture. The SEM images and EDS analysis results in Fig. S12† show that the 3D morphology and element content of the Ni-MAR almost remain unchanged, which illustrates the excellent biocompatibility between cells and Ni-MARs. Therefore, the Ni-MAR can swim and be operated in liquid environments, including water, viscous glycerol–water solution and cell culture medium, except for some acid solutions.

Conclusion

In summary, the current designed Ni-MAR, which has high magnetic content (~90 wt%), is responsible for high-speed swimming and massive cargo carrying. Based on the structure design and parameter optimization, high-fidelity Ni-MARs with various biomimetic morphologies have been fabricated by our "two-photon polymerization + sintering" method. Thanks to its high magnetic content, the Ni-MAR with enhanced magnetic torque is capable of swimming fast and carrying massive cargoes under rotating magnetic fields. The maximum velocity is 12.5 body lengths per second, which is faster than current helical microrobots fabricated by direct laser writing. Besides, a microcube, 200 times heavier, is pushed by a single Ni-MAR to realize translation and rotation motion. As a proof-of-concept demonstration, the high-speed Ni-MAR can swim controllably in fast-flowing fluid inside a microfluidic channel, which offers an alternative scheme for microrobots' propulsion in bloodstream. In addition, the Ni-MAR enables single/multiple cells to be delivered to the target position, which will significantly improve the carrying and therapeutic efficiency in targeted therapy.

Experimental section

Synthesis of Ni-containing photoresist

Acrylic acid (>99%) and 4,4′-bis(diethylamino)benzophenone are purchased from Macklin. Nickel 2-methoxyethoxide (5% w/v in 2-methoxyethoxide) and pentaerythritol triacrylate are purchased from Alfa Aesar. Firstly, 100 mg acrylic acid (AAc, >99%) is added to 1290 mg nickel 2-methoxyethoxide (5% w/v in 2-methoxyethoxide) and manually agitated. Then the obtained solution is held in a vacuum chamber to remove ~60% of 2-methoxyethanol. Finally, 300 mg pentaerythritol triacrylate and 12 mg 4,4′-bis(diethylamino)benzophenone are added into the mixture and agitated using a vortex mixer for 2 min.

Heating profile

After the fabrication by fs-DLW, the Ni-containing polymer-based microhelices are developed in ethanol for 30 min to remove the unpolymerized photoresin. Subsequently, the microhelices are firstly heated under 0.2 L min^{-1} argon in a tube furnace (Hefei Kejing Furnace, China) with a heating profile of 500 °C and a dwelling time of 1 h, then to 750 °C and a dwelling time of 1 h, and finally to 1000 °C and a dwelling time of 1 h (all heating rates are 1 °C min^{-1}). Then the microhelices undergo further reduction under 0.2 L min^{-1} reducing gas (5% H_2, 95% N_2) with a heating profile of 2 °C min^{-1} to 600 °C and a dwelling time of 1 h. The obtained Ni-MAR is immediately evaluated by the following EDS test and swimming test under a magnetic field to avoid the oxidation of nickel.

Magnetic actuation of the Ni-MAR

The Ni-MAR on a glass substrate is released by a home-made microprobe and transferred to a triaxial Helmholtz coil system. The coil system is composed of four parts: data acquisition card controlled by a computer, power amplifier, the Helmholtz coil and the microscopy imaging system. The input signal controlled by the computer is amplified by the power amplifier and enters into the Helmholtz coil to generate a three-dimensional alternating magnetic field. The Ni-MAR can swim in a liquid environment under the actuation of a magnetic field.

Manufacturing of the microfluidic chip

A piece of silica membrane of 250 μm in thickness, 75 mm in length and 25 mm in width is first cut using picosecond lasers (LSP30, Wuhan HGTECH company). A straight channel is produced with a length of 4 cm and a width of 200 μm. Then, the cut silica membrane is plasma-bonded to a glass side, follow by bonding with a silica membrane as a sealing layer. Finally, two PDMS blocks are bonded on the top of the microfluidic chip to hold the inlet and outlet pipe.

Cell culture

HeLa-EGFP cells are obtained from American Type Culture Collection and cultured in a humidified atmosphere at 37 °C with 5% CO_2. The cells are cultured in minimum essential medium supplemented with 10% fetal bovine serum and 1% penicillin/streptomycin (all purchased from Procell Life Science&Technology Co. Ltd.). Before cell seeding, a quartz slide with the as-prepared Ni-MAR is placed in a Petri dish containing 2 mL culture medium. Cells are detached by trypsinization with 0.25% Trypsin–EDTA (Gibco, USA) at 37 °C for 30 s, centrifuged at 1000 rpm for 5 min and resuspended in culture medium at a density of 2×10^6 mL^{-1}, and then seeded onto the quartz slide with the Ni-MAR. The sample is placed in an incubator for 6 h until the cells settle down and adhere to the Ni-MAR, then transferred to the living cell workstation (Leica, inug2-wskm-set) and imaged using a Leica DMI8 Auto microscope for continuous observation of cell growth. The bright field and fluorescence images are recorded every 60 min for 2 days.

Author contributions

R. L. and M. J. contributed equally to this article. R. L., and J. L. designed the experiment. R. L. and M. J. made the organic–inorganic nickel-containing photoresin and fabricated the samples. R. L., M. J., L. Q. and M. L. performed the actuation experiment. R. L., M. J., S. J., B. L. and C. C. analyzed the data and revised the figure. Y. H., W. D., J. L., C. W. and J. C. reviewed and revised the paper.

Conflicts of interest

There are no conflicts to declare.

Acknowledgements

This work was supported by the Major Scientific and Technological Projects in Anhui Province (202103a05020005), the National Natural Science Foundation of China (No. 52075516, 61927814, 52122511), the National Key Research and Development Program of China (No. 2021YFF0502700), the China Postdoctoral Science Foundation (2023M733381), the Joint Fund for New Medicine of USTC (YD2090002016), the Students' Innovation and Entrepreneurship Foundation of USTC (CY2022G09). We acknowledge the Experimental Center of Engineering and Material Sciences at USTC for the fabrication and characterization of samples. This work was partly carried out at the USTC Center for Micro and Nanoscale Research and Fabrication.

References

1 H. Ceylan, I. C. Yasa, O. Yasa, A. F. Tabak, J. Giltinan and M. Sitti, *ACS Nano*, 2019, **13**, 3353–3362.
2 C. Xin, D. Jin, Y. Hu, L. Yang, R. Li, L. Wang, Z. Ren, D. Wang, S. Ji, K. Hu, D. Pan, H. Wu, W. Zhu, Z. Shen, Y. Wang, J. Li, L. Zhang, D. Wu and J. Chu, *ACS Nano*, 2021, **15**, 18048–18059.
3 A. Chen, W. Wang, Z. Mao, Y. He, S. Chen, G. Liu, J. Su, P. Feng, Y. Shi and C. Yan, *Adv. Mater.*, 2023, 2307686.
4 A. Chen, J. Su, Y. Li, H. Zhang, Y. Shi, C. Yan and J. Lu, *Int. J. Extreme Manuf.*, 2023, **5**, 032007.
5 H. Ceylan, N. O. Dogan, I. C. Yasa, M. N. Musaoglu, Z. U. Kulali and M. Sitti, *Sci. Adv.*, 2021, **7**, eabh0273.
6 F. Zhang, J. Zhuang, Z. Li, H. Gong, B. E.-F. de Ávila, Y. Duan, Q. Zhang, J. Zhou, L. Yin, E. Karshalev, W. Gao, V. Nizet, R. H. Fang, L. Zhang and J. Wang, *Nat. Mater.*, 2022, **21**, 1324–1332.
7 Y. Alapan, B. Yigit, O. Beker, A. F. Demirörs and M. Sitti, *Nat. Mater.*, 2019, **18**, 1244–1251.
8 R. Li, Y. Tao, J. Li, D. Jin, C. Xin, S. Ji, C. Wang, Y. Zhang, Y. Hu and D. Wu, *Light: Advanced Manufacturing*, 2023, **4**, 1–13.
9 R. Li, D. Jin, D. Pan, S. Ji, C. Xin, G. Liu, S. Fan, H. Wu, J. Li and Y. Hu, *ACS Nano*, 2020, **14**, 5233–5242.
10 R. Li, C. Zhang, J. Li, Y. Zhang, S. Liu, Y. Hu, S. Jiang, C. Chen, C. Xin and Y. Tao, *Natl. Sci. Rev.*, 2022, **9**, nwac163.
11 O. Yasa, P. Erkoc, Y. Alapan and M. Sitti, *Adv. Mater.*, 2018, **30**, 1804130.
12 V. Garcia-Gradilla, J. Orozco, S. Sattayasamitsathit, F. Soto, F. Kuralay, A. Pourazary, A. Katzenberg, W. Gao, Y. Shen and J. Wang, *ACS Nano*, 2013, **7**, 9232–9240.
13 B. Esteban-Fernández de Ávila, M. A. Lopez-Ramirez, R. Mundaca-Uribe, X. Wei, D. E. Ramírez-Herrera, E. Karshalev, B. Nguyen, R. H. Fang, L. Zhang and J. Wang, *Adv. Mater.*, 2020, **32**, 2000091.
14 S. Ghosh and A. Ghosh, *Sci. Robot.*, 2018, **3**, eaaq0076.
15 H.-R. Jiang, N. Yoshinaga and M. Sano, *Phys. Rev. Lett.*, 2010, **105**, 268302.
16 L. Zhang, J. J. Abbott, L. Dong, B. E. Kratochvil, D. Bell and B. J. Nelson, *Appl. Phys. Lett.*, 2009, **94**, 064107.
17 A. Ghosh and P. Fischer, *Nano Lett.*, 2009, **9**, 2243–2245.
18 D. Gong, N. Celi, L. Xu, D. Zhang and J. Cai, *Mater. Today Chem.*, 2022, **23**, 100694.
19 J. Li, T. Li, T. Xu, M. Kiristi, W. Liu, Z. Wu and J. Wang, *Nano Lett.*, 2015, **15**, 4814–4821.
20 W. Gao, X. Feng, A. Pei, C. R. Kane, R. Tam, C. Hennessy and J. Wang, *Nano Lett.*, 2014, **14**, 305–310.
21 J. Li, S. Sattayasamitsathit, R. Dong, W. Gao, R. Tam, X. Feng, S. Ai and J. Wang, *Nanoscale*, 2014, **6**, 9415–9420.
22 L. Zhang, J. J. Abbott, L. Dong, K. E. Peyer, B. E. Kratochvil, H. Zhang, C. Bergeles and B. J. Nelson, *Nano Lett.*, 2009, **9**, 3663–3667.
23 D. Walker, M. Kubler, K. Morozov, P. Fischer and A. Leshansky, *Nano Lett.*, 2015, **15**, 4412–4416.
24 C. Xin, L. Yang, J. Li, Y. Hu, D. Qian, S. Fan, K. Hu, Z. Cai, H. Wu, D. Wang, D. Wu and J. Chu, *Adv. Mater.*, 2019, **31**, 1808226.
25 S. Tottori, L. Zhang, F. Qiu, K. K. Krawczyk, A. Franco-Obregón and B. J. Nelson, *Adv. Mater.*, 2012, **24**, 811–816.
26 U. Bozuyuk, O. Yasa, I. C. Yasa, H. Ceylan, S. Kizilel and M. Sitti, *ACS Nano*, 2018, **12**, 9617–9625.
27 J. Park, C. Jin, S. Lee, J. Y. Kim and H. Choi, *Adv. Healthcare Mater.*, 2019, **8**, 1900213.
28 C. Peters, O. Ergeneman, P. D. W. García, M. Müller, S. Pané, B. J. Nelson and C. Hierold, *Adv. Funct. Mater.*, 2014, **24**, 5269–5276.
29 X. Wang, X. H. Qin, C. Hu, A. Terzopoulou, X. Z. Chen, T. Y. Huang, K. Maniura-Weber, S. Pané and B. J. Nelson, *Adv. Funct. Mater.*, 2018, **28**, 1804107.
30 X. Wang, X. Z. Chen, C. C. Alcântara, S. Sevim, M. Hoop, A. Terzopoulou, C. De Marco, C. Hu, A. J. de Mello, P. Falcaro, S. Furukawa, B. J. Nelson, J. Puigmartí-Luis and S. Pané, *Adv. Mater.*, 2019, **31**, 1901592.
31 M. Medina-Sánchez, L. Schwarz, A. K. Meyer, F. Hebenstreit and O. G. Schmidt, *Nano Lett.*, 2016, **16**, 555–561.
32 T.-Y. Huang, F. Qiu, H.-W. Tung, X.-B. Chen, B. J. Nelson and M. S. Sakar, *Appl. Phys. Lett.*, 2014, **105**, 114102.
33 C. C. Alcântara, S. Kim, S. Lee, B. Jang, P. Thakolkaran, J. Y. Kim, H. Choi, B. J. Nelson and S. Pané, *Small*, 2019, **15**, 1805006.
34 A. Vyatskikh, S. Delalande, A. Kudo, X. Zhang, C. M. Portela and J. R. Greer, *Nat. Commun.*, 2018, **9**, 593.
35 H.-W. Huang, Q. Chao, M. S. Sakar and B. J. Nelson, *IEEE Robot. Autom. Lett.*, 2017, **2**, 727–732.
36 K. I. Morozov and A. M. Leshansky, *Nanoscale*, 2014, **6**, 12142–12150.
37 E. Kucukal, Y. Man, A. Hill, S. Liu, A. Bode, R. An, J. Kadambi, J. A. Little and U. A. Gurkan, *Am. J. Hematol.*, 2020, **95**, 1246–1256.
38 M. Ranucci, T. Laddomada, M. Ranucci and E. Baryshnikova, *Physiol. Rep.*, 2014, **2**, e12065.
39 J. B. Segur and H. E. Oberstar, *Ind. Eng. Chem.*, 1951, **43**, 2117–2120.
40 T. Li, S. Yu, B. Sun, Y. Li, X. Wang, Y. Pan, C. Song, Y. Ren, Z. Zhang and K. T. Grattan, *Sci. Adv.*, 2023, **9**, eadg4501.

41 M. A. Zeeshan, R. Grisch, E. Pellicer, K. M. Sivaraman, K. E. Peyer, J. Sort, B. Özkale, M. S. Sakar, B. J. Nelson and S. Pané, *Small*, 2014, **10**, 1284–1288.
42 M. Pugsley and R. Tabrizchi, *J. Pharmacol. Toxicol. Methods*, 2000, **44**, 333–340.
43 M. Stücker, V. Baier, T. Reuther, K. Hoffmann, K. Kellam and P. Altmeyer, *Microvasc. Res.*, 1996, **52**, 188–192.
44 L. G. Jorgensen, G. Perko and N. H. Secher, *J. Appl. Phys.*, 1992, **73**, 1825–1830.
45 A. K. Davis, B. Attarha and T. J. Piefke, *J. Insect Sci.*, 2013, **13**, 107.
46 P. S. Segre and E. D. Taylor, *J. Exp. Biol.*, 2019, **222**, jeb199240.
47 R. Kram, *J. Exp. Biol.*, 1996, **199**, 609–612.